

Improvement of Beam Nonuniformity Smoothing Due to X Radiation in Laser-Driven Layered Targets

J. L. Bocher, M. Decroisette, P. A. Holstein, M. Louis-Jacquet, B. Meyer, A. Salères, and G. Thiell

Commissariat à l'Énergie Atomique, Centre d'Études de Limeil-Valenton, F-94190 Villeneuve-Saint-Georges, France

(Received 11 October 1983)

The effect of laser-beam spatial modulations on plane targets is analyzed as a function of modulation scale length and target material by means of x-ray shadowgraphy. At short laser wavelength it is shown that lateral energy smoothing is clearly improved because of the strong x-ray emission from the irradiated high- Z side of layered targets. The results, interpreted in terms of radiation-driven thermal transport, are in agreement with numerical simulations.

PACS numbers: 52.50.Jm, 44.40.+a, 52.25.Fi, 52.55.Mg

Laser-plasma interaction with short laser wavelength offers advantages such as better energy deposition, increased x-ray self-emission, and reduced plasma instabilities. Nevertheless, a major question in laser fusion is the symmetry of spherical target implosions which has to be better than a few percent in order to achieve the high required densities.^{1,2} If hydrodynamic instabilities do not arise, pressure asymmetries at the ablation surface are due to a nonuniform laser energy deposition. Lateral diffusion is classically known to reduce the nonuniformities by $\exp(-2\pi D/l)$, where D is the distance between deposition region and ablation surface and l the nonuniformity scale length.² Analytical models predict that D scales as λ^n where λ is the laser wavelength and $n=2.6$ or 4.6 in spherical² or plane³ geometry, respectively. Therefore short laser wavelengths, although attractive for hydrodynamic efficiency, would not favor implosion symmetry.^{2,4} Alternative ways have been proposed to improve the situation for directly driven implosion: gradual shift to shorter wavelength during implosion,⁵ increase of laser intensity on small targets with constant $l\lambda^2$,⁶ use of low-density foams,⁷ or improvement of laser uniformity by induced spatial incoherence.⁸ Nonuniformity smoothing has been experimentally studied versus irradiance for 1.06- and 0.53- μm laser wavelengths.^{9,10} In this paper, we present an experimental study of nonuniformity smoothing for 0.35 μm as a function of irradiance modulation scale length and target material. First evidence is given of an improved smoothing due to x-radiation transport in high- Z –low- Z layered targets.

The Nd laser we use delivers 60 J in 1-nsec, 1.06- μm pulses. After frequency tripling through two potassium dihydrogen phosphate crystals, the 0.35- μm energy is typically 20 J.¹¹ The beam is focused onto disk targets with a $f/6.7$, 600-mm-

focal-length lens. The absorption rate in the range of irradiance 10^{13} – 2×10^{14} W cm^{-2} is close to 95%. Irradiance modulations are induced by inserting different sets of opaque horizontal strips in the incident beam. From microdensitograms of focal-spot images in vacuum we deduce that the spatial wavelength l is 30 to 100 μm and the modulation rate

$$\gamma_I = (I_{\max} - I_{\min}) / (I_{\max} + I_{\min})$$

equals 0.7 ± 0.1 . A 20-J, 1.06- μm laser beam is focused on a copper target providing us with an x-ray backlighting source of 0.9 nsec full width at half maximum in duration. Spatially resolved x-ray shadowgrams are recorded with an 18- μm pinhole camera through a 9- μm -thick aluminum filter. The recorded spectral range is 1.2–1.56 keV. The probing axis is parallel to the target surface along the direction of the strips. Deduced from x-ray absorption data, the density corresponding to the shadow limit for targets accelerated over a 200- μm diameter is close to 0.15 g cm^{-2} .^{9,11} Two broadband K -edge x-ray spectrometers, equipped with vacuum diodes and p - i - n diodes, give the front spectral emission from the plasma in the range 0.1–30 keV.¹² The disk targets, 500 μm in diameter, are made either of aluminum (25 μm thick), or gold (0.5–4 μm thick), or aluminum (7 μm) coated with a gold layer (0–8500 Å). For the thickest targets, the probing delay time is 4 nsec after the maximum of the laser pulse. For the thinnest targets the fast decompression requires a delay time of 2.5 nsec. Because of the x-ray pulse duration the shadow smearing is important, but microdensitograms along the laser axis show that the uncertainty on target location is not greater than 25%.

Figure 1 shows typical shadowgrams of accelerated targets. Microdensitograms of the superimposed x-ray self-emission from the irradiated side [Fig.

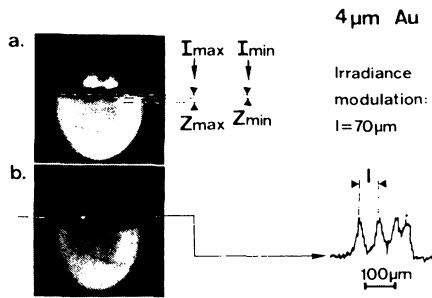


FIG. 1. Typical x-ray shadowgrams.

1(b)] reproduced the irradiance modulations. Z_{min} and Z_{max} are the distances traveled by the rear portions of the target corresponding to I_{min} and I_{max} , respectively. The modulation rate of the rear side velocity is

$$\gamma_v = \gamma_z = (Z_{max} - Z_{min}) / (Z_{max} + Z_{min}).$$

First, we assume that the rear velocity modulations are equal to the ablation-pressure modulations. Then, deduced from the ablation-pressure scaling¹³ $P_a \propto I^{0.78}$, the pressure modulation rate without smoothing is $\gamma_a = 0.6 \pm 0.1$ for $\gamma_I = 0.7 \pm 0.1$. Finally, the smoothing factor is written as $\Gamma = \gamma_z / \gamma_a$ and can be directly compared to theoretical evaluations.

Variations of Γ as a function of the wave number $k = 2\pi/l$ are plotted in Fig. 2 for Al and Au thick targets. Comparison is done with the smoothing factor derived from an analytical treatment of a transverse perturbation propagating between critical and ablation surfaces.³ The application has to be cautiously considered since the model is steady state, the energy is assumed to be deposited at the critical density, and the x radiation is not taken into account. Nevertheless, a slightly more pronounced smoothing is observed in Al targets. In spite of a markedly larger x-ray conversion rate in gold (40% as against 5% in aluminum; Fig. 3), the radiative

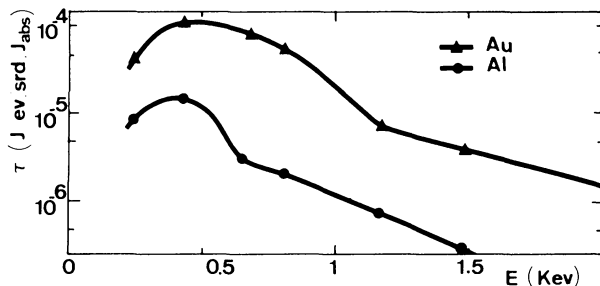


FIG. 3. X-ray energy distributions for thick targets. The laser irradiance is $10^{14} \text{ W cm}^{-2}$.

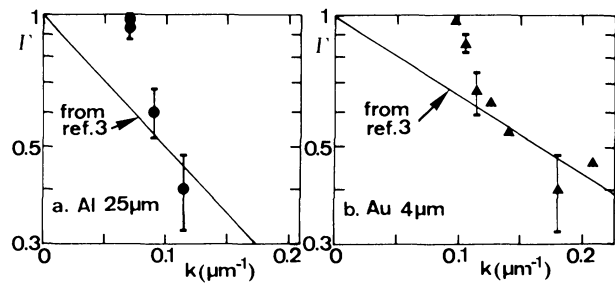


FIG. 2. Smoothing factor Γ as a function of the modulation wave number k for thick targets. The laser irradiance I_{max} is $5 \times 10^{13} \text{ W cm}^{-2}$.

transfer is not the prevailing process of energy smoothing for thick targets. A strong self-absorption in gold limits the inward propagation of the leading radiative component of the thermal front.^{14,15} We tried to improve the radiative transfer by associating a thin gold ablative layer, providing a large inward radiative heating, and a low-Z substrate, allowing a farther x-ray penetration.

Figure 4, curve *a* presents experimental variations of Γ for gold-coated aluminum disks, $7 \mu\text{m}$ thick, versus the thickness of the gold layer h and for $l = 50 \mu\text{m}$. An optimum in smoothing is clearly evident for $h \sim 0.5 \mu\text{m}$. Obviously, a gold thickness greater than a few times the ablated layer ($2200 \pm 200 \text{ \AA}$) prevents the x-ray emission from reaching the Al target. The results obtained for bare gold targets (Fig. 4, curve *b*) show that there is no significant smoothing for targets thicker than $1.5 \mu\text{m}$. Conversely, for $h < 0.75 \mu\text{m}$, the target explodes and the observed smoothing is carried out with densities close to 0.15 g cm^{-3} . On the other hand, comparing the motion of targets of the same areal density (for example $10\text{-}\mu\text{m}$ Al and $0.5\text{-}\mu\text{m}$

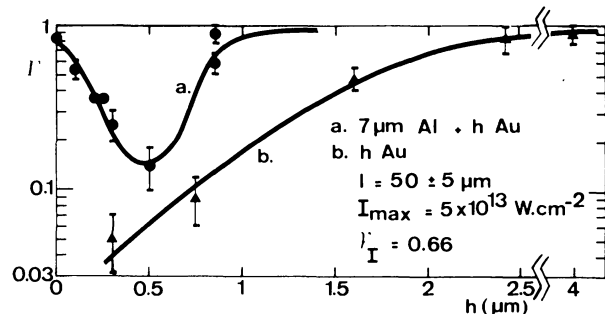


FIG. 4. Smoothing factor Γ for (a) gold-coated aluminum targets vs the thickness of the gold layer; (b) bare gold targets vs the target thickness.

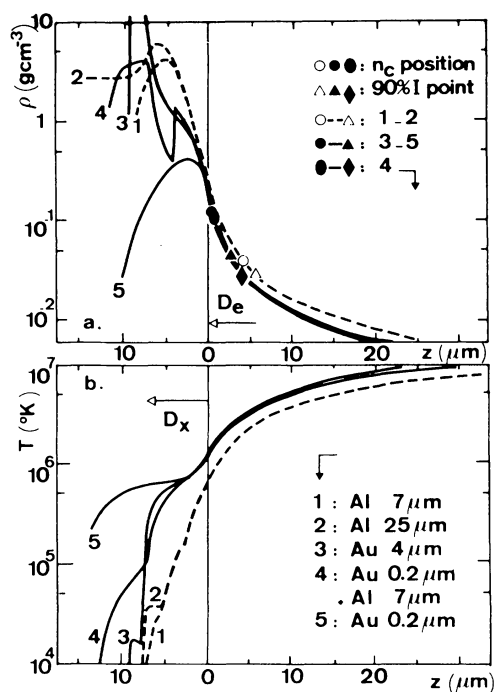


FIG. 5. Numerical density and temperature profiles along the laser axis. The inward radiative energy flux equals the electron energy flux for $z=0$. The density step in curve 4 corresponds to the Al-Au interface.

Au on 7- μm Al), we checked that the hydrodynamic efficiency is not altered in layered targets and rises up to 20%.

Obviously, numerical simulations describing the evolution of the rear-side modulations should be done with a two-dimensional (2D) code. Nevertheless, a 1D hydrodynamic Lagrangian code¹⁶ allows us to approach the parameters controlling the energy smoothing during the time of the energy deposition. The 2D aspect is taken into account by introduction of the distance D in the expression $\Gamma = \exp(-kD)$ derived from the simple model of lateral energy diffusion.² The treatment of the x-ray emission uses a multigroup method. In accordance with the measured x-ray spectrum, the suprathermal electron preheat is assumed to be negligible. The thermal flux limiter, f , equals 0.04. Five significant density and temperature profiles are presented in Fig. 5 at 300 psec after the laser peak. The distance D cannot be simply described as the distance between critical and ablation surfaces. Especially for short laser wavelengths and high- Z materials, energy deposition does not occur at critical (n_c , circles in Fig. 5). As an example, we reported the point where 90% of the incident energy has been absorbed (triangles in Fig. 5). Furthermore,

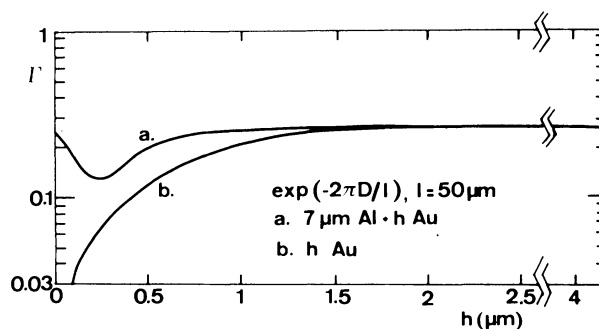


FIG. 6. Numerical smoothing factor Γ vs gold thickness.

D overlaps two regions with different transport mechanisms: First, energy propagation towards higher-density matter is dominated by electron conduction over a distance D_e ; then, beyond critical, radiative transport prevails and the radiation thermal front drives the shock wave^{14,15} over a distance D_x . This region is responsible for the emission of the low-energy component of the x-ray spectrum (Fig. 3). For more convenient comparison, each profile in Fig. 5 has been plotted in such a way that the origin on the laser axis is the point where the inward radiative energy flux equals the electron energy flux. This method emphasizes that the density and temperature profiles in the electronic region only depend on the irradiated material. Because of the strong x-ray conversion in gold, the temperature in the radiative region is higher than in aluminum (curves 3 and 2, respectively), but the temperature gradient is very much steeper and the distance moved by the shock wave is only about 1 μm greater. So a more pronounced smoothing in 25- μm -thick Al targets (Fig. 2) is mainly attributed to the difference on the energy deposition locations. Furthermore, it is clearly shown that for a coated target (0.2- μm Au on 7- μm Al, curve 4), the gold layer appears as a radiative energy reservoir (it is still acting after the end of the laser pulse). The penetration of the thermal front in aluminum is deeper than in the thick gold target and about twice as deep as in a 7- μm -thick, bare aluminum target (curve 1). Besides, from simple expressions of mean free paths, it can be seen that the transverse smoothing in the radiative region will be more efficient than in the electron region. Finally, a thin gold target (0.2 μm , curve 5) behaves as an exploding pusher: The density at the end of the laser pulse is too low to achieve high fuel compressions. The smoothing factor of the "cloudy day" model, $\exp(-kD)$, is plotted in Fig. 6. Here, D has been chosen as the total distance between energy deposi-

tion and thermal front. A qualitative accordance with the experimental behavior is observed: The difference is ascribed to the 1D description.

To summarize, the pressure uniformity required in the context of laser fusion seems difficult to achieve at $\lambda = 0.35 \mu\text{m}$. Increasing the laser intensity to recover the smoothing obtained at $\lambda = 1.06 \mu\text{m}$ ¹⁰ would lead to a reappearance of the plasma instabilities.² However, we have shown that the smoothing could be improved because of the effect of radiative heating on hydrodynamics provided that we use high- Z -low- Z layered targets. We evidenced an improvement by a factor 4 or 5 without noticeable reduction of the hydrodynamic efficiency. Layered shells with such a structure can be considered in the scheme of spherical implosions of large-diameter pellets (1 mm) driven with high-energy multibeam lasers (a few times 10 kJ). A more suitable numerical treatment obviously requires 2D simulations, possibly taking account of self-focusing and hydrodynamic instabilities, and may need to clearly dissociate the respective smoothing efficiency of electron and radiative transfer.

The authors want to thank Dr. J. Coutant for fruitful discussions and wish to acknowledge the help of the laser team and the target fabrication group. The technical assistance of A. Fourel, G. Nierat, G. Pantigny, and A. Queffelec was greatly appreciated.

¹J. Nuckolls, L. Wood, A. Thiessen, and G. Zimmerman, *Nature (London)* **239**, 139 (1972).

²S. E. Bodner, *J. Fusion Energy* **1**, 221 (1981); J. H. Gardner and S. E. Bodner, *Phys. Rev. Lett.* **47**, 1137 (1981).

³W. M. Manheimer, D. G. Colombant, and J. H. Gardner, *Phys. Fluids* **25**, 1144 (1982).

⁴C. E. Max, J. D. Lindl, and W. L. Mead, *Nucl. Fusion* **23**, 131 (1983).

⁵A. R. Thiessen and J. H. Nuckolls, University of California Radiation Laboratory Report No. UCRL 78459, 1976 (unpublished).

⁶E. Fabre, *Bull. Am. Phys. Soc.* **25**, 992 (1980).

⁷K. Okada *et al.*, *Appl. Phys. Lett.* **42**, 231 (1983).

⁸R. H. Lehmburg and S. P. Obenschain, *Opt. Commun.* **46**, 27 (1983).

⁹S. P. Obenschain, J. Grün, B. H. Ripin, and E. A. McLean, *Phys. Rev. Lett.* **46**, 1402 (1981); S. P. Obenschain *et al.*, *Phys. Rev. Lett.* **30**, 44 (1983).

¹⁰A. J. Cole *et al.*, *J. Phys. D* **15**, 1689 (1982).

¹¹G. Thiell, B. Meyer, P. Aussage, and X. Fortin, *Opt. Commun.* **46**, 305 (1983).

¹²D. Babonneau *et al.*, in *Laser Interaction and Related Plasma Phenomena*, edited by H. Hora and G. H. Miley (Plenum, New York, 1983), Vol. 6.

¹³B. Meyer and G. Thiell, *Phys. Fluids* (to be published).

¹⁴H. D. Shay *et al.*, *Phys. Fluids* **21**, 1640 (1978).

¹⁵D. Duston, R. W. Clark, J. Davis, and J. P. Apruzese, *Phys. Rev. A* **27**, 1441 (1983).

¹⁶C. Bayer *et al.*, in *Laser Interaction and Related Plasma Phenomena*, edited by H. Hora and G. H. Miley (Plenum, New York, 1983), Vol. 6.

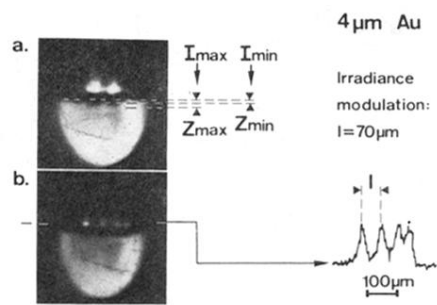


FIG. 1. Typical x-ray shadowgrams.